www.acsnano.org

# Prediction of Three-Metal Cluster Catalysts on Two-Dimensional W<sub>2</sub>N<sub>3</sub> Support with Integrated Descriptors for Electrocatalytic Nitrogen Reduction

Siyu Chen,<sup>‡</sup> Yongqi Gao,<sup>‡</sup> Wugang Wang,<sup>‡</sup> Oleg V. Prezhdo,\* and Lai Xu\*



Downloaded via UNIV OF SOUTHERN CALIFORNIA on March 4, 2023 at 04:42:21 (UTC). See https://pubs.acs.org/sharingguidelines for options on how to legitimately share published articles.

Cite This: ACS Nano 2023, 17, 1522-1532



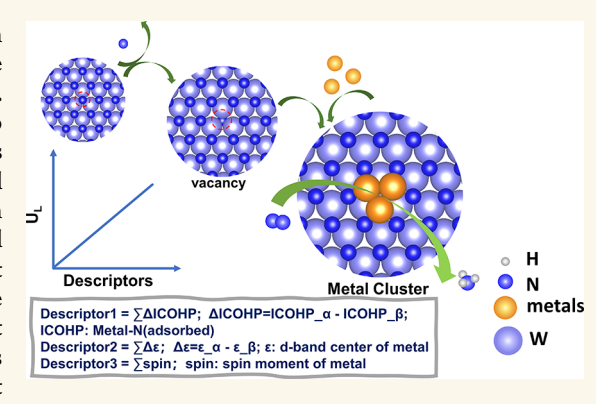
**ACCESS** 

Metrics & More

Article Recommendations

Supporting Information

ABSTRACT: In the electrocatalytic nitrogen reduction reaction (NRR), nitrogen  $(N_2)$  is chemically inert, it is difficult to break the triple bond, and the subsequent protonation step is very challenging. Suitable catalysts with high selectivity and high activity are needed to promote the electrocatalytic NRR. We screen a large number of clusters composed of three metal atoms embedded into a two-dimensional metal nitride,  $W_2N_3$ , with a N vacancy, and calculate the reaction energetics. The VNiCu cluster has the best catalytic activity among all the catalysts proposed so far. The Fe<sub>3</sub> and Fe<sub>2</sub>Co clusters are excellent catalysts as well. In all cases, spin polarization is needed to observe the catalytic effect. We establish the optimal NRR path and confirm that it remains unchanged in the presence of a solvent. We find three groups of descriptors that can well predict the materials' properties and exhibit linear relationships with the NRR limiting potential.



KEYWORDS: NRR catalysis, Two-dimensional materials, Metal cluster, High-throughput screening, Descriptor

### **INTRODUCTION**

Ammonia is important since it is one of the raw materials used in the modern chemical industry. However, the predominant way to synthesize it on a large scale is the Haber-Bosch method, which combines nitrogen and hydrogen directly to form ammonia gas at high temperature and pressure. Although some known Fe-based catalysts<sup>2</sup> have reduced the pressure and temperature required for the reaction to some extent, the actual pressure and temperature are still higher than expected, which results in a huge consumption of energy. The search for efficient, low-cost, and environmentally friendly nitrogen reduction methods and catalysts has become a significant topics. Electrocatalytic reduction of nitrogen is currently expected to be one of the methods which can replace the traditional ammonia synthesis.<sup>3-6</sup> We can turn clean energy, such as solar energy, tidal energy, or wind energy, into electricity to produce ammonia, greatly reducing industrial environmental pollution and energy problems. Considering that the electrocatalytic nitrogen reduction reaction (NRR) process mostly occurs in aqueous solution, it will inevitably be disrupted by the competing hydrogen evolution reaction (HER). Therefore, it is necessary to find a suitable catalyst for

the NRR which can maintain a high activity to promote breaking of the N≡N triple bond and ensure a high selectivity for the NRR.

After the Geim group successfully isolated graphene in 2004, multiple classes of two-dimensional atomic crystal materials (such as MXenes, transition metal nitrides, transition metal carbides, <sup>9–12</sup> and two-dimensional metal sulfides represented by molybdenum disulfide (MoS<sub>2</sub>), <sup>13,14</sup> transition-metal-modified g-C<sub>3</sub>N<sub>4</sub>, <sup>15</sup> etc.) have been proposed or discovered in succession. Because two-dimensional materials have an atomic width in a certain direction, the high specific surface facilitates catalytic reactions, since only surface catalysis occurs in bulk materials. Many materials mentioned above have been proved to be excellent catalysts for the HER, oxygen evolution reaction/oxygen reduction

Received: October 24, 2022 Accepted: January 4, 2023 Published: January 6, 2023





reaction, carbon dioxide reduction, and nitrogen reduction. Transition metal nitrides (TMNs) are a relatively recent class of two-dimensional material. Due to their excellent conductivity, high degree of hardness, and favorable two-dimensional structure, there have been reports  $^{16,17}$  on the synthesis and catalytic performance of TMNs, especially  $W_2N_3.^{18,19}$  Currently, the control of the electronic structure on the substrate surface relies on formation of nitrogen vacancies for the NRR catalytic studies.  $^{19}$ 

Herein, we introduce metal clusters on a nitrogen vacancy of TMNs and explore the NRR performance. There are experiments proving that W<sub>2</sub>N<sub>3</sub> can be used in the NRR, <sup>19</sup> and the N vacancy on the transition metal has the important property of adsorbing dinitrogen molecules.<sup>20</sup> The structural stability of W2N3 containing vacancies is also proved experimentally. 19 The development of single-atom and cluster catalysts<sup>21,22</sup> shows that it is feasible to create active sites centered on single atoms or atom clusters on substrates for various catalytic reactions. 23,24 Single-atom 25,26 and doubleatom<sup>27</sup> catalysts have made great progress in recent years and have many attractive advantages. We continue to try tri-atom cluster catalysts based on these excellent works. Experimentally, Holland et al. have created a series of multinuclear iron complexes to simulate nitrogenase, 28 which proves that multinuclear clusters can effectively weaken the N≡N triple bond at room temperature. Moreover, Liang and co-workers have synthesized Fe-Cu heterogeneous clusters for NRR.<sup>29</sup> The introduction of dissimilar metals may have a positive impact on the catalytic properties of the clusters.<sup>30</sup> Single-element metal clusters are reported often,<sup>31,32</sup> but differentelement metal clusters systems are studied much less. Only the catalytic properties of clusters formed by common atoms such as Fe and Cu are reported.<sup>33–35</sup>

In recent years, advances in computer performance and related algorithms have made it possible to carry out highthroughput calculations. Large-scale screening of different substrates, as well as different doping atoms and doping methods, has helped in the discovery of many catalysts with excellent performance. Descriptors such as d-band center, 36,37 electronegativity,38 and number of valence or orbital electrons<sup>39,40</sup> can be used to characterize catalysts with a single physical quantity. Current machine-learning algorithms include Least Absolute Shrinkage and Selection Operator (LASSO), 41,42 Sure Independence Screening and Sparsifying Operator (SISSO),<sup>43</sup> random forest algorithms, neural network algorithms, and so on,<sup>44,45</sup> all of which have made important contributions in relevant fields.<sup>46</sup> Our group used LASSO to train descriptors including rotation angle of heterojunction ( $\theta$ ), average bond length (1), distance between upper and lower heterojunctions (d), and ratio of band gap between two heterojunction components ( $\lambda$ ) to describe the catalytic performance.<sup>47–50</sup> Basic properties of metal atoms (see the Supporting Information (SI), Table S5) and electronic structure information were comprehensively considered by LASSO. In this paper, on the basis of a large number of clusterdoping calculations, descriptors with a good linear relationship with  $U_L$  (limiting potential) are found, including ICOHP\_ $\alpha$ -ICOHP  $\beta$  (ICOHP: integrated crystal orbital Hamilton population) between metal and N2, spin moment, and dband center gap (spin-up d-band center  $(\varepsilon \, \alpha)$  minus spindown d-band center  $(\varepsilon_{-}\beta)$ ), providing theoretical prediction and guidance for NRR catalyst performance.

Preliminary screening was carried out on the basis of both formation energy and nitrogen adsorption vs H adsorption selectivity. The structure of the model is shown in Figure 1. In

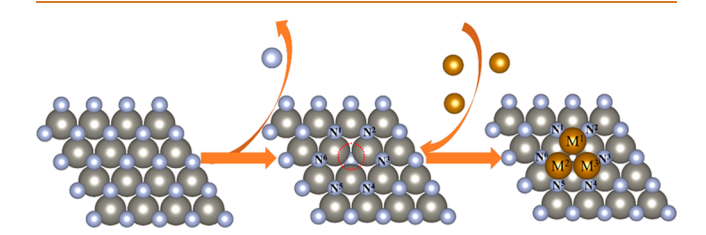


Figure 1. Structural construction of cluster@NV-W2N3.

the end, 56 systems were selected, and the full reaction path calculation was performed for these systems. Based on a large number of reaction full-path calculations, we determined the best performance for AAA, AAB, and ABC systems was shown by Fe<sub>3</sub>@NV-W<sub>2</sub>N<sub>3</sub>, Fe<sub>2</sub>Co@NV-W<sub>2</sub>N<sub>3</sub>, and VNiCu@NV-W<sub>2</sub>N<sub>3</sub>, respectively. Detailed electronic structure calculations, including COHP and density of state calculations, were performed for the three best systems. The difference in spin polarization of metals leads to different coupling between metals, and between metal and N<sub>2</sub>, which affects catalytic performance. According to the LASSO analysis, we found descriptors that have a good linear relationship with U<sub>L</sub>, providing an alternative direction for finding efficient descriptors.

### **RESULTS AND DISCUSSION**

We calculated the surface energy of low-index surfaces and surfaces with different terminations (SI Table S1). Among them, the (001) surface is the most stable surface structure, so our vacancy structure is also selected in the (001) surface structure. The surface energy (E\_surf) can be calculated as

$$E_{surf} = (E_{slab} - N * E_{bulk})/2A$$

where E\_surf is the surface energy, E\_slab is the energy of the slab supercell, E\_bulk is the bulk energy per atom, N is the number of atoms in the slab, and A is the surface area of the slab.

In order to explore the possibility of catalytic NRR after modification of  $W_2N_3$  by different metal clusters, homogeneous and heterogeneous clusters composed of different metal atoms were introduced into the nitrogen vacancies in  $W_2N_3$  ( $W_2N_3$ -NV). Starting from a single metal cluster (AAA), metal clusters composed of two or more metal atoms were constructed, their catalytic performance was evaluated, and the electronic structure changes from nitrogen adsorption to ammonia reduction were analyzed. Qiao et al. 19 reported the possibility and synthesis of nitrogen vacancies in  $W_2N_3$ . The vacancies formed on the surface of  $W_2N_3$  are surrounded by six nitrogen atoms in the basal position. Three metal atoms are embedded into the vacancy, where each metal atom is coordinated with two nitrogen atoms, and the metal clusters are fixed in the middle of the void in a triangular form.

The clusters are composed of transition metals in various combinations. We classify the clusters as homogeneous (clusters of the same atoms) and heterogeneous (clusters with different metal atoms). There are AAA (three identical metal atoms), AAB (two identical and one different metal atom), and ABC (three different atoms) cluster types. Twenty-eight structures for AAA type clusters, such as Fe<sub>3</sub>, Ni<sub>3</sub>, and

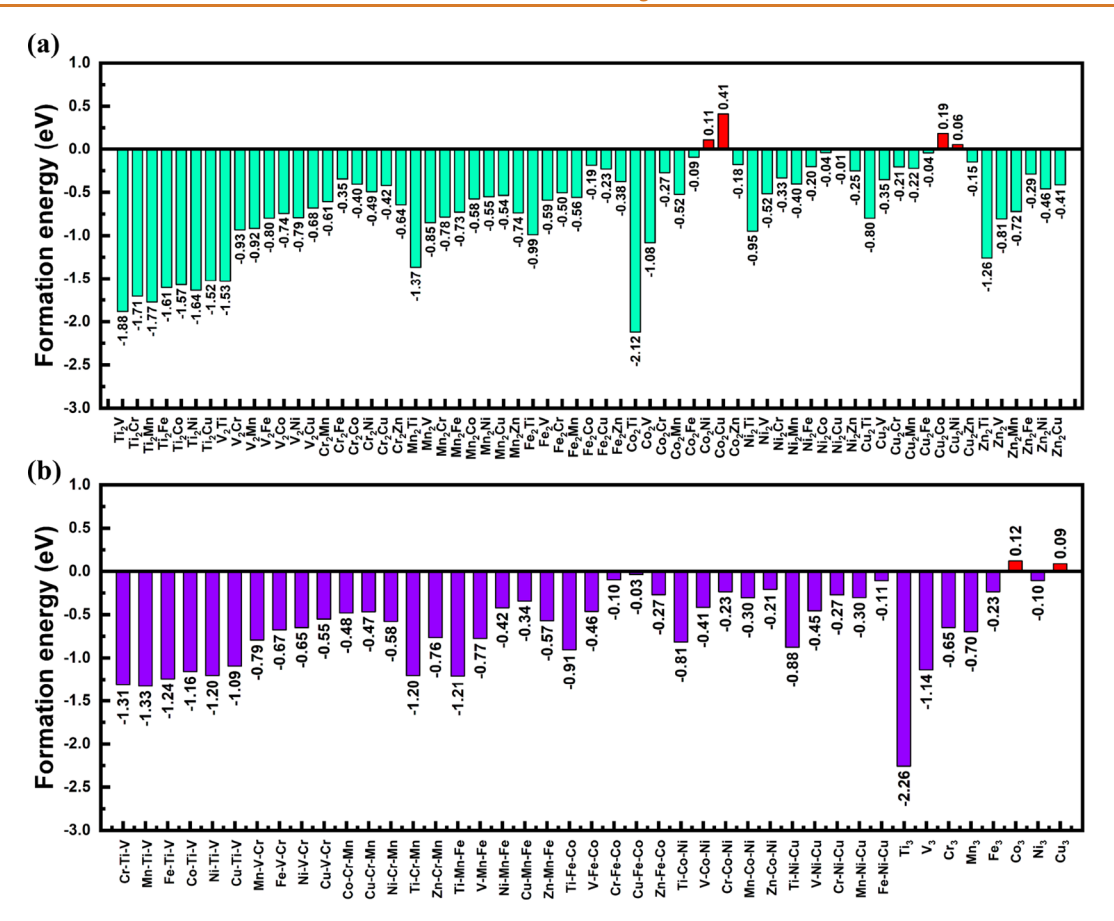


Figure 2. Bar charts of formation energies of metal cluster@NV-W<sub>2</sub>N<sub>3</sub> for (a) type AAB and (b) types ABC and AAA. Red indicates positive adsorption energy.

 $Cr_3$ , 71 structures for AAB type clusters, such as  $Fe_2Co$  and  $Mn_2Ni$ , and 35 structures for ABC type clusters, such as TiCrMn, were optimized. Eight structures for the AAA type, 65 structures of the AAB type, and 35 structures of the ABC type clusters are left after the optimization.

The optimization results show that most of the cluster structures can be well anchored among the six nitrogen atoms, and each metal not only forms clusters with two adjacent metals but also has coordination with two N atoms. In order to verify whether the optimized systems are thermodynamically stable, we calculated the formation energy for each system. The formation energy of a cluster anchored to the base is defined by the following formula:

$$\begin{split} E_f &= [E(cluster/NV-W_2N_3) - E(NV-W_2N_3) \\ &- (E(M_1) + E(M_2) + E(M_3))]/3 \end{split}$$

where  $E(\text{cluster/NV-W}_2N_3)$  represents the total energy of structural optimization when metal clusters are anchored at  $W_2N_3$  containing N vacancies, and  $E(\text{NV-W}_2N_3)$  represents the total energy of structural optimization for  $W_2N_3$  with N vacancies, while  $E(M_n)$  (n=1,2,3) represents the energy of each metal, which comes from the energy averaging for each atom of the most stable crystal structure of each metal after optimization. Figure 2 shows the formation energies of different metal clusters. The formation energy data can be found in the SI, Tables S2.1, S2.2, and S2.3. The formation energy of the AAA type clusters is relatively low, while the energy of formation of the AAB or ABC type clusters is mostly negative and the structures tend to be more stable. In the AAA

type, the formation energies of the  $Co_3$  and  $Cu_3$  systems are positive, indicating that they are not stable. In the AAB type, the  $Co_2Ni$ ,  $Co_2Cu$ ,  $Cu_2Co$ , and  $Cu_2Ni$  systems were removed. The formation energies of the heterogeneous ABC systems were all negative, indicating that they were stable. Hence, there are 102 systems left.

Only systems with negative formation energies are considered further, since they are thermodynamically stable after the clusters are anchored on the base. In order to further verify the stability of the clusters anchored on the base, we tested three systems,  $Fe_3$ ,  $Fe_2Co$ , and VNiCu, from the AAA, AAB, and ABC classes, respectively, using AIMD. The structures of the  $Fe_2Co$  system at 300 K and the VNiCu and  $Fe_2Co$  systems at 800 K are slightly deformed, but the amplitude of the energy fluctuation is small, and the overall structure is stable (SI Figure S2).

In the process of NRR, the competitive HER needs to be considered. Therefore, it is necessary to compare which species is more likely to adsorb on the reaction site of the clusters,  $N_2$  or H. We conducted nitrogen adsorption and H adsorption tests on the thermodynamically stable structures, and obtained  $G(N_2 \ ads)$  and  $G(H \ ads)$ :

$$G(N_2 - ads) = G(*N_2) - G(*) - G(N_2)$$

$$G(H_ads) = G(^*H) - G(^*) - 1/2 G(H_2)$$

A positive value of the adsorption energy means that the base cannot adsorb  $N_2$  or H spontaneously, while a negative value means that the base can spontaneously adsorb nitrogen

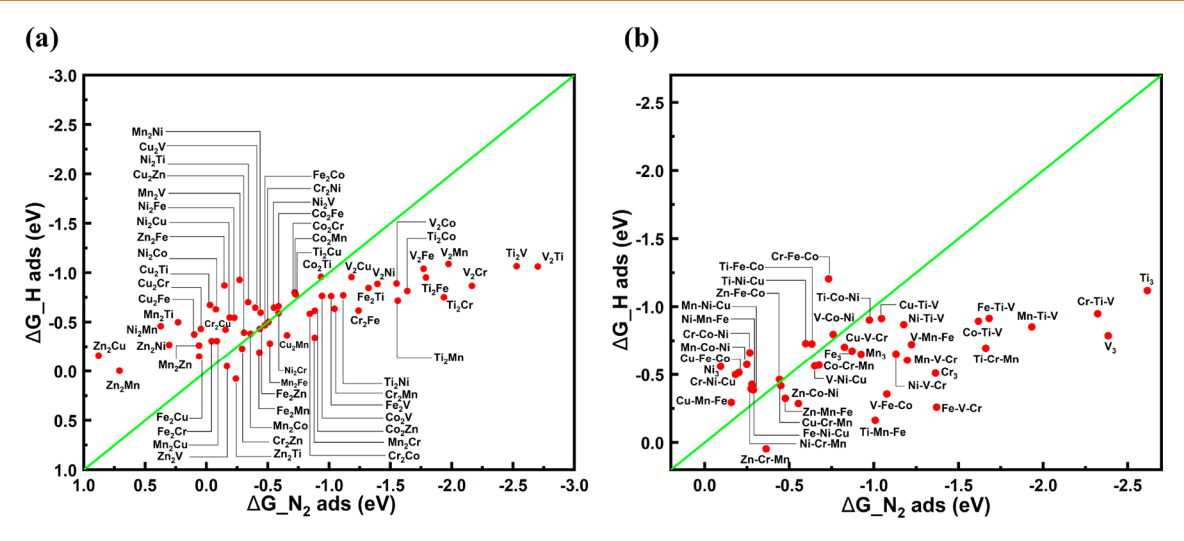


Figure 3. Nitrogen adsorption energy and H adsorption energy of metal cluster@NV-W<sub>2</sub>N<sub>3</sub>. (a) Selected comparison between the nitrogen and H adsorption energies on systems of the AAB type. (b) Selected comparison between the nitrogen and H adsorption energies on systems of the ABC and AAA types. Points below the green line correspond to the nitrogen adsorption energy being less than the H adsorption energy; points above the green line have the nitrogen adsorption energy greater than the H adsorption energy.

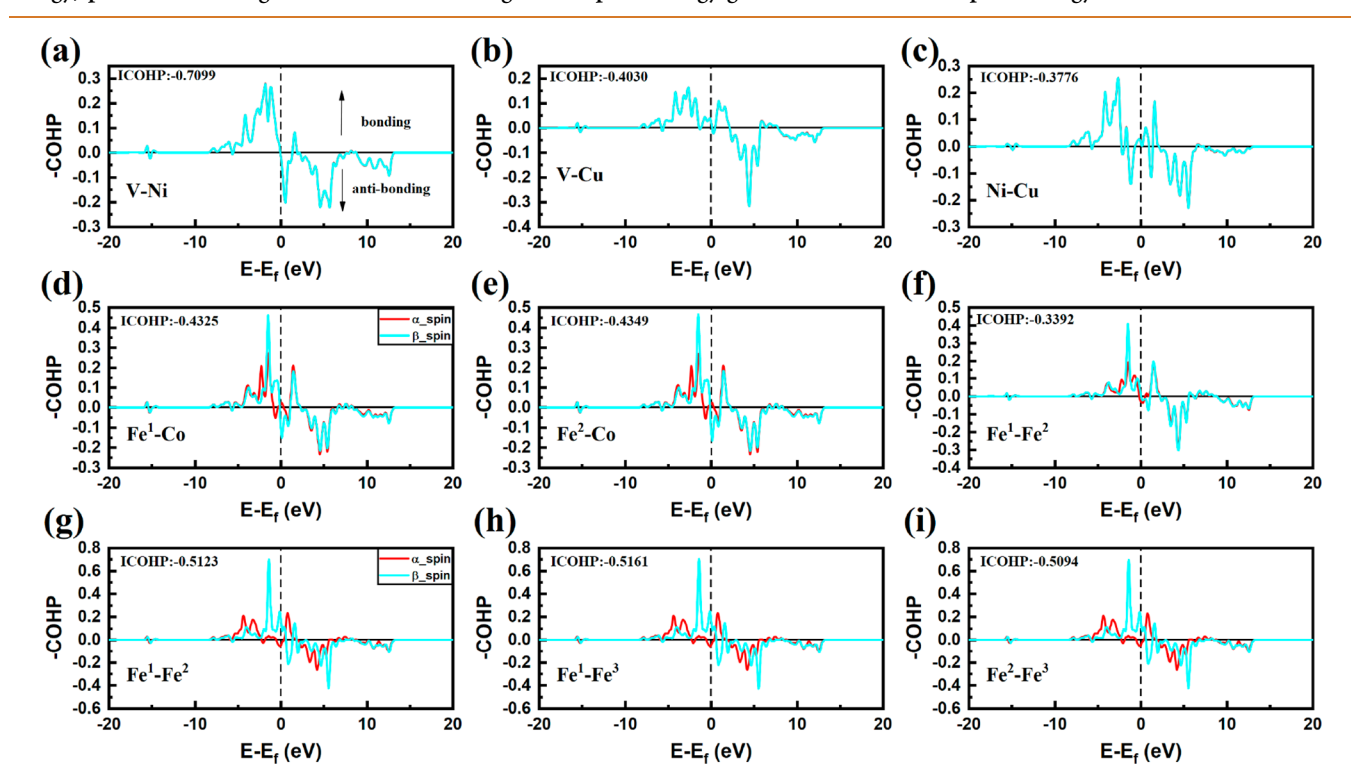


Figure 4. COHP of different intermetallic d orbitals in (a-c) the VNiCu system, (d-f) the Fe<sub>2</sub>Co system, and (g-i) the Fe<sub>3</sub> system.

molecules or H atoms. After removing the systems that do not adsorb  $N_2$ , the nitrogen and H adsorption energies of the remaining systems are compared. When  $G(N_2\_ads) > G(H\_ads)$ , the substrate tends to adsorb H. In other words, H will occupy the reaction site first and make nitrogen adsorption difficult. When  $G(N_2\_ads) < G(H\_ads)$ , the base has better selectivity to the nitrogen.

The results of the competitive reaction screening for various clusters are shown in Figure 3. 46 systems from the AAB, ABC, and AAA classes have been removed, as they have positive  $N_2$  adsorption energies (specific data can be found in the SI, Tables S3.1 and S3.2). Other systems are eliminated since they preferentially adsorb free H rather than nitrogen molecules.

Finally, all 56 stable systems were evaluated for their catalytic selectivity.

According to the triangular adsorption configuration of clusters on the base, there are many reasonable nitrogen adsorption modes, but the strengths of these adsorptions are different. One of the cluster systems was chosen to verify which mode of nitrogen adsorption on clusters is more stable. The adsorption modes can be divided into single-metal adsorption, double-metal adsorption, and triple-metal adsorptions. For single-metal adsorption, nitrogen falls on only one metal in the metal cluster (SI, Figure S1a, S1f; S1d, S1i). Double-metal adsorption occurs when nitrogen falls on the edge of the metal cluster triangle, and the metals on both sides

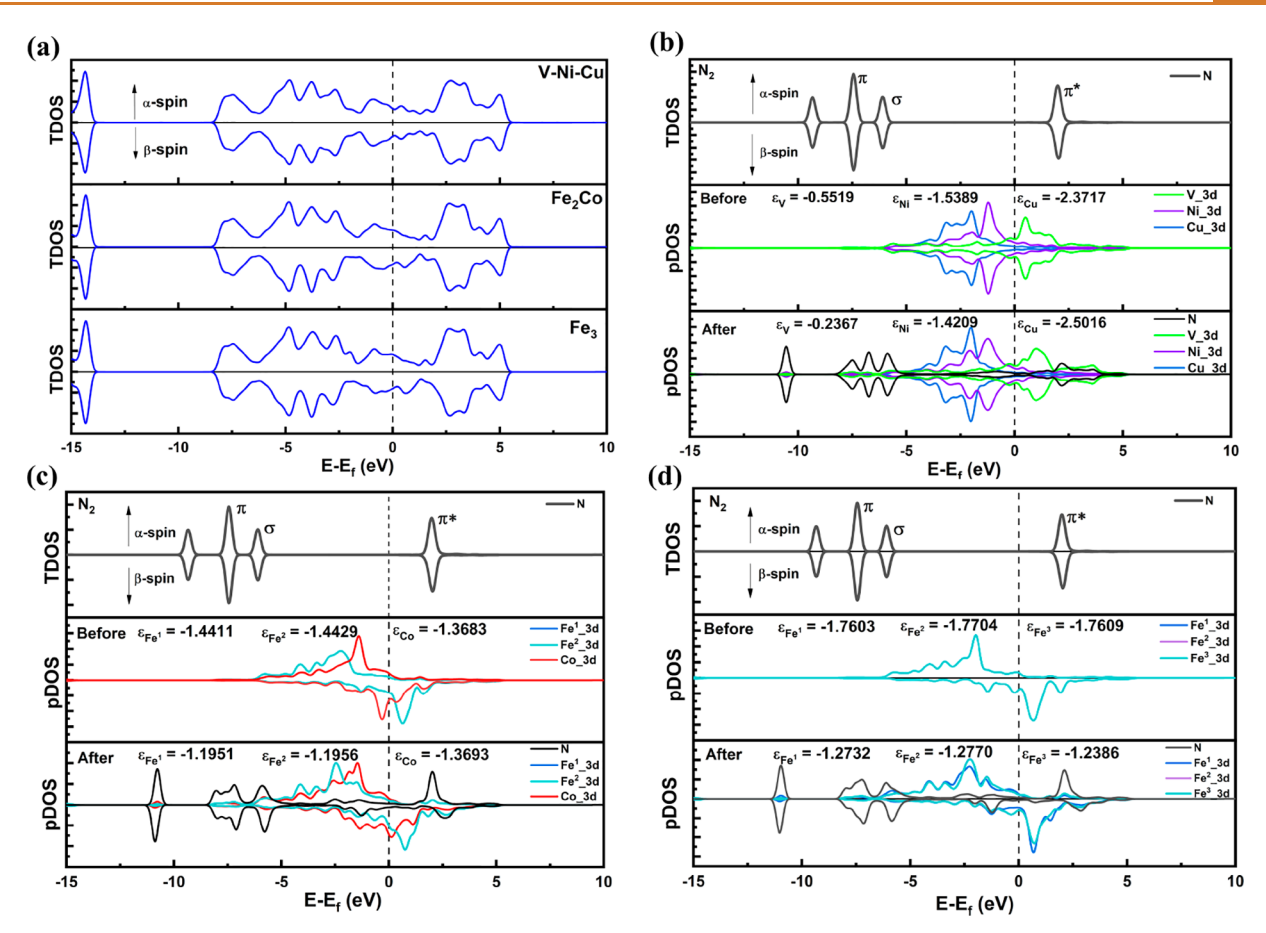


Figure 5. (a) TDOS of VNiCu,  $Fe_2Co$ , and  $Fe_3$  systems. (b-d) DOS before and after  $N_2$  adsorption with base clusters. Comparison of the changes of three metal d orbitals and nitrogen pDOS in the VNiCu (b),  $Fe_2Co$  (c), and (d)  $Fe_3$  systems before and after adsorption, in which the pDOS diagram curves of Fe atoms at two different positions before adsorption are completely identical in the  $Fe_2Co$  system and the pDOS diagrams of the three Fe atoms before adsorption are identical and overlapped in the  $Fe_3$  system. The top image in Figure b-d is the TDOS of  $N_2$ .

clamp the two ends of nitrogen like pliers, to form the adsorption configuration (Figure S1b, S1g; S1e, S1j). For triple-metal adsorption, nitrogen falls at the center of the cluster and is captured by three metals at the same time (Figure S1c, S1h). The nitrogen molecule is located on top of the triangular cluster. The structures of different adsorption configurations are shown in Figure S1. When we ran adsorption tests on other systems, we found that in all the optimized structures nitrogen binds to three metal atoms.

Through geometric optimization of these adsorption modes, the adsorption energy of each configuration was calculated. It can be seen that nitrogen adsorption in the center of the three metal atoms is the most stable adsorption mode. From the overall adsorption energy, the adsorption capacity for nitrogen of a single metal atom is smaller than that of multiple metal atoms. For example, the adsorption energy for nitrogen of a single Co atom is only -0.39 eV. The nitrogen side-on adsorption energy on Fe is -0.77 eV. The adsorption energies for nitrogen interacting with two and three metal atoms are much more negative. In order to explore the joint interaction of trimetals, we calculated the reaction mechanisms of NRR for 56 systems. The energy data for  $N_2$ ,  $H_2$ , and  $NH_3$  involved in the calculation are shown in the SI, Table S6.

According to the energy calculation of the intermediates, the reaction free energy diagram of NRR can be obtained. The maximum free energy is the potential-limiting step to reflect

the catalytic performance of the system, and its theoretical limiting potential can be obtained from  $U_L = -\Delta G max/e$ . (The potential-determining step and  $U_L$  are shown in the SI, Table S4.) After obtaining the limiting potential, we need to find the cluster combination anchored on  $W_2N_3$ -NV with the best NRR catalytic performance.  $U_L$  in the 56 systems ranges from -1.44~V to -0.35~V (SI Figures S3–S7).

Analysis of the electronic structure of different cluster systems during nitrogen adsorption and subsequent protonation step reactions helps us to find the interaction between the cluster systems and the adsorbate. DOS (density of states), differential charge, spin density, and COHP (crystal orbital Hamiltonian population) analyses were performed on the  $Fe_3@NV-W_2N_3$ ,  $Fe_2Co@NV-W_2N_3$ , and  $VNiCu@NV-W_2N_3$  systems with better NRR catalytic performance.

Figure 4 shows the COHP between doping metals. In the SI, Figures S8, S9, and S10 show COHP between doping metal and nitrogen in the substrate in different systems before nitrogen adsorption. ICOHP is the quantity representing the bond strength between atoms. The more negative the bond strength is, the stronger the bond is. Analysis of the data shows that the bonds between the metal atoms and the N atoms of the substrate are relatively strong, indicating that the metal can be stably embedded in the N environment. Metals exist in clusters, and metal—metal interactions are not as strong as those of metal—N of the substrate. Compared with the other

two systems, the VNiCu system has slight spin polarization. The contributions of spin\_ $\alpha$  and spin\_ $\beta$  are overlapping, and the contributions of the two orbitals are roughly the same. In the VNiCu system,  $V-N^1$  is -2.2908 and  $V-N^2$  is -2.4809;  $Ni-N^3$  is -0.9493 and  $Ni-N^4$  is -0.6076; and  $Cu-N^5$  is -0.4684 and Cu-N<sup>6</sup> is -0.6104 (Figure S8). There is a great difference between metal-metal and metal-N interactions. The bonds between metals are weaker than those with the substrate. For example, V-Ni is -0.7099, V-Cu is -0.4030, and Ni-Cu is -0.3776; they are all weaker than those of metal-substrate. For the Fe<sub>3</sub> system (Figure 4g,h,i), the interactions of the doped metals are completely consistent, being contributed by two  $\alpha$  bonding peaks and two  $\alpha$ antibonding peaks below the Fermi level. Due to spin polarization, the  $\beta$  orbital does not overlap with the  $\alpha$  orbital. The  $\beta$  orbital is located with two bonding peaks below the Fermi level and two antibonding peaks above the Fermi level. Similar bonding is also seen in Fe<sub>2</sub>Co, due to spin polarization. However, for the VNiCu system, since no spin polarization occurs, the contributions of  $\alpha$  and  $\beta$  to bonding and antibonding are consistent—the bonding is mainly contributed by the  $\alpha$  and  $\beta$  orbitals at -2.5 eV below the Fermi level, and the antibonding is contributed by orbitals at -1 eV below the Fermi level and orbitals above the Fermi level.

As shown in Figure 5a, we calculated the total density of states (TDOS) for VNiCu@NV-W2N3, Fe2Co@NV-W2N3, and Fe<sub>3</sub>@NV-W<sub>2</sub>N<sub>3</sub>. It can be seen from the figure that all the three structures are conductors, so they are suitable for electrocatalysis. The partial density of states (pDOS) diagrams of the VNiCu@NV-W2N3, Fe2Co@NV-W2N3, and Fe3@ NV-W<sub>2</sub>N<sub>3</sub> metal substrates before and after N<sub>2</sub> adsorption were analyzed and compared (Figure 5b-d). The d orbital contribution of the metals was selected. The DOS diagrams show the distribution of  $\alpha$  and  $\beta$  orbitals, with  $\alpha$  orbitals above y = 0 and  $\beta$  orbitals below y = 0. The  $\alpha$  and  $\beta$  orbitals of Fe and Co demonstrate asymmetry due to their spin polarization. But this spin polarization is not obvious in the VNiCu system. In Figure 5a, Ni and Cu, and V and Ni atoms'  $\alpha$  and  $\beta$  orbital peaks almost overlap, indicating that the interactions between Ni-Cu and V-Ni are stronger than V-Cu. The Fe and Co peaks of Fe<sub>2</sub>Co@NV-W<sub>2</sub>N<sub>3</sub> in Figure 5b are not exactly the same and only partially overlapped. The  $\alpha$  and  $\beta$  peaks of the three Fe atoms of Fe<sub>3</sub>@NV-W<sub>2</sub>N<sub>3</sub> in Figure 5c are perfectly coincident, indicating the strongest interaction. After nitrogen adsorption, the DOS of each atom in the cluster also changes. Figure 5a-c shows the two  $\pi^*$  orbitals of nitrogen and the metal  $\beta$  orbital, which have been shifted to 2.5 eV due to spin polarization, forming another d- $\pi^*$  orbital. The remaining nitrogen orbitals are  $\sigma$  and  $\pi$  bond orbitals. They are dispersed with the metal orbitals below the Fermi level to form d- $\sigma$  and  $d-\pi$  bond occupation orbitals. The transfer of  $\beta$  electrons of the metal's d orbital to the d- $\pi^*$  orbital, a combination of nitrogen molecules and the metal, results in nitrogen receiving too many  $\beta$  electrons. The  $\alpha$  orbital of nitrogen itself has no obvious energy-matching relationship with the  $\alpha$  orbital of metal; hence, there is no interaction, and it will not accept the  $\alpha$ electron of the metal. As a result, the number of  $\beta$  electrons is more than that of  $\alpha$  electrons after nitrogen adsorption on the cluster, and electrons are urgently needed to pair them, making the subsequent protonation step process possible. The difference of d-band centers between the spin\_  $\alpha$  and spin\_  $\beta$  states affects the catalytic performance of NRR. In other words, the spin polarization of the metal eventually activates

nitrogen. DOS calculation results before and after adsorption show that the d-p hybrid interaction between metal and N leads to the redistribution of electrons, and the d-band center moves up. The metal-N bonding is enhanced, and the N-N bond is weakened, except for Cu in VNiCu, since Cu does not directly contact N and form bonds (Figure S11). The COHP after N<sub>2</sub> adsorption on the substrate (Figures S11–S13) shows that N<sub>2</sub> has a strong interaction with the clusters. Figure S14 shows the ICOHP before and after N<sub>2</sub> adsorption. After N<sub>2</sub> adsorption, the value of ICOHP between metal and substrate N changes little: only the Ni-N value in the VNiCu system changes greatly, and the N2 adsorption has little effect on the metal-substrate N bond. The value of ICOHP between metals decreases due to formation of another metal-N bond, and the bond strength decreases. The N-N ICOHP decreases greatly, because the formed metal-N bond activates the N-N triple bond, and the bond strength decreases. In the case of Fe<sub>3</sub>, nitrogen molecules have stable bonds with the metal atoms: ICOHP of Fe<sup>1</sup>-N<sup>2</sup> is -1.1614, Fe<sup>2</sup>-N<sup>1</sup> is -1.7256, and Fe<sup>3</sup>- $N^2$  is -1.1697, which shows that  $N_2$  can be stably adsorbed on the surface. Among the three systems, the shift of the d-band center of Fe3 is the biggest, the metal-molecular interaction of Fe<sub>3</sub> is stronger, and the bond strength of NN after adsorption is the weakest, with the ICOHP of N-N being -9.2935. Hence, its NRR activity is the best.

In order to verify and further analyze the electron transfer trend after nitrogen adsorption, the spin density and the difference in charge density on the structure after adsorption were analyzed (Figure S15 and Figure S16). The results are consistent with the DOS analysis. Figure S15 shows that electrons are transferred from electron-rich metal cluster centers to nitrogen molecules (yellow is electron gain region, blue is electron loss region). Figure S16 shows that there are more  $\beta$ -state electrons on the N<sub>2</sub> molecule and more  $\alpha$ -state electrons on the metal, which indicates that part of the  $\beta$ electrons of the metal are transferred to the d- $\pi^*$  orbital formed by the metal and N. However, it is special for the VNiCu@NV-W2N3 system, where DOS and spin density indicate this system has little spin polarization. Hence, the  $\beta$ electron density on N is less than for the other two systems. Therefore, it can be seen from Figure \$16c,f that there is a small change in spin density near the V, Ni, and Cu atoms, which is consistent with the information provided by the DOS diagram shown in Figure 5a.

To further characterize nitrogen activation, we calculated and analyzed Bader charges. First, we calculated the Bader charge of each part before and after N2 adsorption (Figure S17). The figures shows that electrons of the metal cluster transfer to N<sub>2</sub> and form metal-N bonds after N<sub>2</sub> adsorption. This leads to weakening of the bonds between metal atoms, which is consistent with the results of the above ICOHP analyses. In addition, we found that N around the metal cluster can balance the electron transfer on the metal. After N<sub>2</sub> adsorption, the electrons on other atoms in the surrounding environment are indirectly transferred to the metal cluster and provided to N2. The N around the metal is essentially unchanged before and after the adsorption. The cluster transfers electrons to N<sub>2</sub>. When the electrons transferred by the cluster are insufficient, N in the surrounding environment plays an intermediate role in transferring electrons to the cluster. This phenomenon is more obvious in the Fe<sub>2</sub>Co and Fe<sub>3</sub> systems. Therefore, in the catalytic process, clusters and their environment jointly promote the catalytic reaction. In

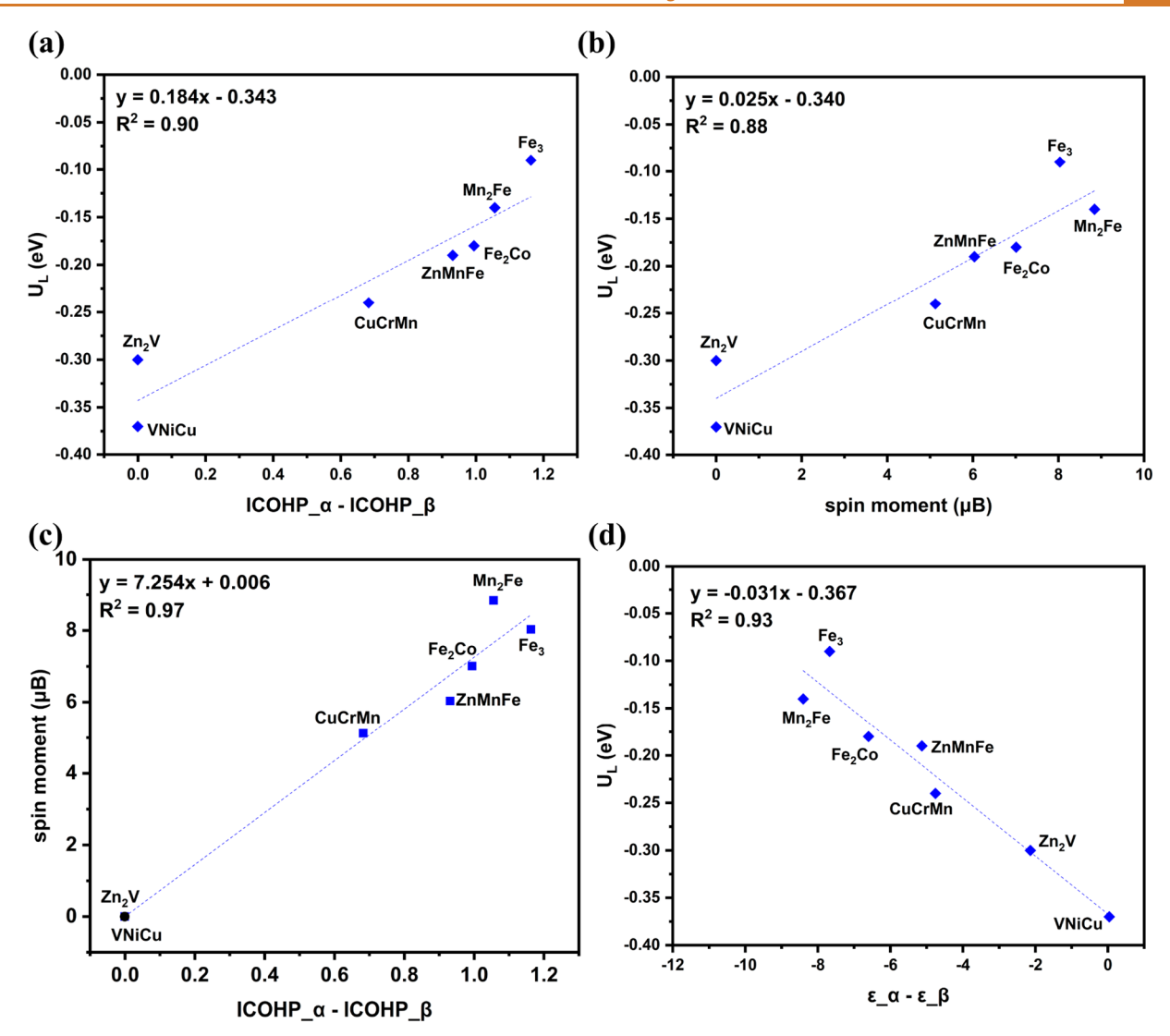


Figure 6. (a) Linear regression relationship between ICOHP\_ $\alpha$ -ICOHP\_ $\beta$  (the sum of three metals) and  $U_L$ . (b) Linear regression relationship between spin moment (the sum of three metals) and  $U_L$ . (c) Linear regression relationship between ICOHP\_ $\alpha$ -ICOHP\_ $\beta$  and spin moment. (d) Linear regression relationship between d-band center gap (the sum of three metals) and  $U_L$ .

addition, we calculated the change of the Bader charge along the reaction pathway. The black, green, and red dots and lines in Figure S18 show the Bader charge changes of each doped metal in the three systems before and after nitrogen adsorption as well as in the subsequent hydrogenation steps. The blue and dark blue dots show how the charges of nitrogen and the adsorbent change between hydrogenation steps. As analyzed by DOS and COHP above, after nitrogen adsorption, part of the metal electrons will be transferred to the coupling orbital between metal and nitrogen. As shown in Figure S18a, for \*\*-\*N-\*N, i.e., in the process of nitrogen adsorption, the charge value of each doped metal drops and the charge value of the nitrogen molecule rises. Nitrogen in the normal state has 0 valence, and electrons are obtained after adsorption. In the first step to the third step in the hydrogenation process, metal charges change little. Thus, there is not much electron transfer between the metal and nitrogen. However, the charge of nitrogen is increasing all the time. Therefore, the charge of nitrogen comes mostly from the H atom. By the time the fourth H atom is added, the charge of nitrogen decreases and the charge of the metal increases, suggesting that after the fourth hydrogen adsorption the N-N bond is greatly

weakened. N transfers part of the electrons to the metal, and the electronic interaction within N-N decreases.

Concise descriptors can help us find high-performance catalysts easily. Thus, we selected 7 systems from the above path-screened systems to find descriptors. Then, we collected the electronic structure information, analyzed the relationship between various parameters and U<sub>L</sub> through LASSO, and combined the parameters with high weight. Finally, we found descriptors that can well describe the NRR properties of the material in this way. As shown in Figure 6a, U<sub>L</sub> is closely related to the sum of ICOHP of metal-N after N<sub>2</sub> adsorption. The larger the difference between ICOHP  $\alpha$  and ICOHP  $\beta$ , the smaller the value of UL, the better the NRR performance, and  $R^2 = 0.90$ . The difference between  $\alpha$  and  $\beta$  states reflects the influence of metal spin moment. Therefore, we also investigated the relationship between spin moment and U<sub>L</sub>. As shown in Figure 6b, the larger the sum of spin moments of the metal, the smaller the  $U_L$  value, and  $R^2 = 0.88$ . Hence, we can find that the high spin moment of the base metal can better activate N2 to promote NRR and reduce the barrier of the potential-determining step (PDS). At the same time, as we deduced, spin moment is closely related to the difference

between the  $\alpha$  and  $\beta$  states of ICOHP, and its R<sup>2</sup> reaches 0.97 (Figure 6c). We also found that there is a better linear relationship between the difference of the d-band center in two different states (d-band center gap) and  $U_L$ , and its fitting  $R^2$  = 0.93 (Figure 6d). The larger the gap, the lower the U<sub>L</sub> value, which also proves that the spin polarization of the material is conducive to promoting NRR.

In order to better match the experimental environment, we selected the systems with excellent performance after screening to further calculate the influence of the solvent environment on catalysis, and we considered various possible paths. We selected the three lowest barriers from ABC, AAB, and ABC—respectively VNiCu, Fe<sub>2</sub>Co, and Fe<sub>3</sub>—and calculated various possible pathways modified by solvation (Figure 7a).

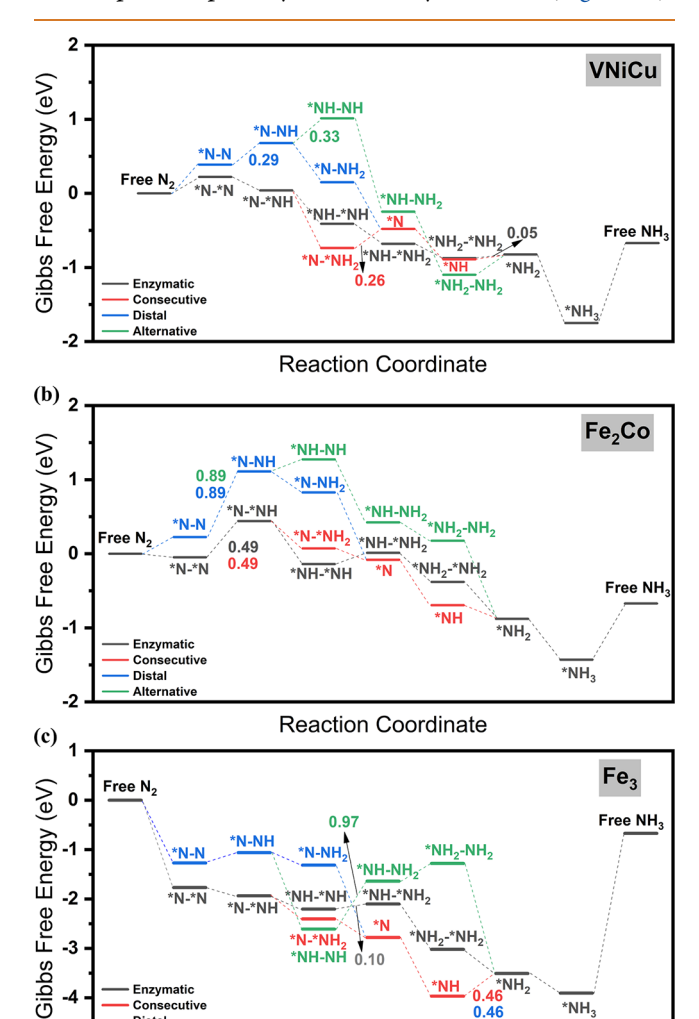


Figure 7. Enzymatic, consecutive, distal, and alternative reaction pathways for NRR of (a) VNiCu, (b) Fe<sub>2</sub>Co, and (c) Fe<sub>3</sub>.

**Reaction Coordinate** 

Consecutive

Distal

The  $U_L$  values of the three systems are -0.05 V, -0.49 V, and -0.10 V in the enzymatic pathway. It has good competitiveness with the NRR catalyst proposed at present (Table S7). Compared with the data without solvation, the U<sub>L</sub> value of the VNiCu system decreases, and the U<sub>L</sub> values of the Fe<sub>2</sub>Co and Fe<sub>3</sub> systems both increase. This is mainly due to the different effects on different adsorbed species in the solvation environment. In addition, we also considered the influence of the pH value. The changes of the NRR reaction energy

barrier of the three systems at different pH values are shown in Figure S19 in the SI. As pH increases, the energy barrier of PDS also increases.

We further considered the solvation effects and charge effects of the selected system on the NRR reaction. Grand canonical potential kinetics<sup>51,52</sup> was used to calculate the reaction energy barrier of the NRR. The energetics computed by this method are in good agreement with experimental conditions. Figure S20 in the SI shows the NRR energetics of the Fe<sub>3</sub> system in the constant potential method (cpm) and the charge-neutral method (cnm). Under the cpm, the energy change trends of most protonation steps are similar. The barrier of the PDS decreases, rather than rises, which may be due to the fact that in the solution and charge environment H is more easily adsorbed on N, forming N-H.

### **CONCLUSIONS**

In this paper, we built clusters composed of three atoms loaded on the surface of the two-dimensional material W<sub>2</sub>N<sub>3</sub> with vacancies. We screened all the possible cluster combinations, selected the clusters that meet the stability requirements, and selected the system with good selectivity to carry out the full reaction path calculations. Large-scale system path calculations show that VNiCu@NV-W2N3 has the lowest UL of only -0.05 V. It has the best performance among the catalysts proposed to date. In addition, the excellent performance of our system is verified by the calculation of grand canonical potential kinetics. Then, we studied the DOS and COHP and found that spin polarization plays an important role in nitrogen adsorption. It can effectively weaken the N≡N triple bond, which is beneficial to the subsequent hydrogenation reaction. Combined with the results of LASSO, we propose descriptors that can predict NRR U<sub>L</sub>, greatly reducing the computational cost.

### **METHODS**

In this study, VASP (Vienna Ab initio simulation package) was used to calculate density functional theory. The projector-augmented-wave (PAW) was set to calculate the exchange energy between ions and electrons; the PBE (Perdew-Burke-Ernzerhof)-GGA (generalized gradient approximation) algorithm was used for exchange and correction interaction between electrons. The energy convergence threshold is set to  $10^{-5}$  eV, and the force convergence threshold is set to 0.05 eV/A; a 450 eV plane wave cutoff energy was used for structural optimization and frequency calculation. points are used in structural optimization, single-point energy calculation, primary atomic and molecular dynamics, and subsequent electron state density and crystal orbital Hamiltonian population calculations. In addition, the DFT-D3 method is used to describe the possible van der Waals forces in the structure.

The difference of Gibbs free energy at each step is given by the formula  $\Delta G = \Delta E_{\rm H} + \Delta E_{\rm ZPE} - T\Delta S_{\rm H}$ , where  $\Delta E_{\rm ZPE}$  refers to the zeropoint energy of each step,  $\Delta S_{\rm H}$  refers to the entropy of the adsorbate (these values can be obtained by VASP's zero-point energy correction function), and  $\Delta E_{\rm H}$  refers to every step after the structure optimization (can be directly obtained by VASP energy).  $^{60}T$  stands for temperature, and the temperature at each step is set at 298.15 K.

All structures are stored in a = 11.7236 Å, b = 11.7236 Å, c = 22.4984 Å;  $\alpha = 90^{\circ}$ ,  $\beta = 90^{\circ}$ ,  $\gamma = 120^{\circ}$ . The VASPKIT<sup>61</sup> was used to post-process the data of electronic state density and differential charge density. Lobster software was used to calculate the crystal orbital Hamilton population in conjunction with VASP. 62-65 We also considered the case of electrochemical catalysis of catalysts in aqueous solution using VASPsol module<sup>66</sup> and the CANDEL<sup>67</sup> implicit solvation model in JDFTx, then we used the grand canonical DFT<sup>68</sup> in JDFTx to perform the constant-potential calculations.

\*NH<sub>3</sub>

### ASSOCIATED CONTENT

### Supporting Information

The Supporting Information is available free of charge at https://pubs.acs.org/doi/10.1021/acsnano.2c10607.

Surface, formation, and atom adsorption energies; adsorption structures; potential-determining steps; basic properties of metal atoms; zero-point energy and pH corrections; ab initio MD data; energy barrier diagrams; crystal orbital Hamilton population analyses; spin and charge densities; Bader charges; comparison with other catalysts (PDF)

### **AUTHOR INFORMATION**

### **Corresponding Authors**

Oleg V. Prezhdo — Department of Chemistry, University of Southern California, Los Angeles, California 90089, United States; orcid.org/0000-0002-5140-7500;

Email: prezhdo@usc.edu

Lai Xu — Institute of Functional Nano & Soft Materials (FUNSOM), Joint International Research Laboratory of Carbon-Based Functional Materials and Devices, Soochow University, Suzhou 215123 Jiangsu, P.R. China; Jiangsu Key Laboratory for Carbon-Based Functional Materials & Devices, Soochow University, Suzhou 215123 Jiangsu, P.R. China; orcid.org/0000-0003-2473-3359; Email: xulai15@suda.edu.cn

### **Authors**

Siyu Chen — Institute of Functional Nano & Soft Materials (FUNSOM), Joint International Research Laboratory of Carbon-Based Functional Materials and Devices, Soochow University, Suzhou 215123 Jiangsu, P.R. China; Jiangsu Key Laboratory for Carbon-Based Functional Materials & Devices, Soochow University, Suzhou 215123 Jiangsu, P.R. China

Yongqi Gao — Institute of Functional Nano & Soft Materials (FUNSOM), Joint International Research Laboratory of Carbon-Based Functional Materials and Devices, Soochow University, Suzhou 215123 Jiangsu, P.R. China; Jiangsu Key Laboratory for Carbon-Based Functional Materials & Devices, Soochow University, Suzhou 215123 Jiangsu, P.R. China

Wugang Wang — Institute of Functional Nano & Soft Materials (FUNSOM), Joint International Research Laboratory of Carbon-Based Functional Materials and Devices, Soochow University, Suzhou 215123 Jiangsu, P.R. China; Jiangsu Key Laboratory for Carbon-Based Functional Materials & Devices, Soochow University, Suzhou 215123 Jiangsu, P.R. China

Complete contact information is available at: https://pubs.acs.org/10.1021/acsnano.2c10607

### **Author Contributions**

<sup>‡</sup>S.C., Y.G., and W.W. contributed equally. L.X. conceived and designed the project, provided key step guidance, verified the data, and made extensive revisions to this paper. O.V.P. guided the project and worked on material presentation and manuscript text. S.C., Y.G., and W.W. performed DFT calculations. L.X., Y.G., and S.C. co-wrote the paper.

### Notes

The authors declare no competing financial interest.

### **ACKNOWLEDGMENTS**

L.X. acknowledges financial support from the National Natural Science Foundation of China-Major Research Plan (91961120), National Natural Science Foundation of China-General Program (22273063), and Major Program in Jiangsu University Natural Science Research (21KJA150004). O.V.P. acknowledges support from the U.S. National Science Foundation (CHE-2154367). This work is also supported by Suzhou Key Laboratory of Functional Nano & Soft Materials, Collaborative Innovation Center of Suzhou Nano Science & Technology, the 111 Project.

### **REFERENCES**

- (1) Haber, F.; Van Oordt, G. Über die Bildung von Ammoniak aus den Elementen. Z. Anorg. Chem. 1905, 47 (1), 42–44.
- (2) Kandemir, T.; Schuster, M. E.; Senyshyn, A.; Behrens, M.; Schlogl, R. The Haber-Bosch process revisited: on the real structure and stability of "ammonia iron" under working conditions. *Angew. Chem., Int. Ed. Engl.* **2013**, 52 (48), 12723–6.
- (3) Guo, Y.; Wang, T.; Yang, Q.; Li, X.; Li, H.; Wang, Y.; Jiao, T.; Huang, Z.; Dong, B.; Zhang, W.; Fan, J.; Zhi, C. Highly Efficient Electrochemical Reduction of Nitrogen to Ammonia on Surface Termination Modified Ti<sub>3</sub>C<sub>2</sub>T<sub>x</sub> MXene Nanosheets. *ACS Nano* **2020**, 14 (7), 9089–9097.
- (4) Zhang, N.; Shang, J.; Deng, X.; Cai, L.; Long, R.; Xiong, Y.; Chai, Y. Governing Interlayer Strain in Bismuth Nanocrystals for Efficient Ammonia Electrosynthesis from Nitrate Reduction. *ACS Nano* **2022**, *16* (3), 4795–4804.
- (5) Chen, X.; Guo, Y.; Du, X.; Zeng, Y.; Chu, J.; Gong, C.; Huang, J.; Fan, C.; Wang, X.; Xiong, J. Atomic Structure Modification for Electrochemical Nitrogen Reduction to Ammonia. *Adv. Energy Mater.* **2020**, *10* (3), 1903172.
- (6) Cui, X. Y.; Tang, C.; Zhang, Q. A Review of Electrocatalytic Reduction of Dinitrogen to Ammonia under Ambient Conditions. *Adv. Energy Mater.* **2018**, 8 (22), 1800369.
- (7) Novoselov, K. S.; Geim, A. K.; Morozov, S. V.; Jiang, D.; Zhang, Y.; Dubonos, S. V.; Grigorieva, I. V.; Firsov, A. A. Electric field effect in atomically thin carbon films. *Science* **2004**, *306* (5696), 666–9.
- (8) Li, X. F.; Li, Q. K.; Cheng, J.; Liu, L.; Yan, Q.; Wu, Y.; Zhang, X. H.; Wang, Z. Y.; Qiu, Q.; Luo, Y. Conversion of Dinitrogen to Ammonia by FeN<sub>3</sub>-Embedded Graphene. *J. Am. Chem. Soc.* **2016**, *138* (28), 8706–9.
- (9) Pang, S. Y.; Wong, Y. T.; Yuan, S.; Liu, Y.; Tsang, M. K.; Yang, Z.; Huang, H.; Wong, W. T.; Hao, J. Universal Strategy for HF-Free Facile and Rapid Synthesis of Two-dimensional MXenes as Multifunctional Energy Materials. *J. Am. Chem. Soc.* **2019**, *141* (24), 9610–9616.
- (10) Johnson, L. R.; Sridhar, S.; Zhang, L.; Fredrickson, K. D.; Raman, A. S.; Jang, J.; Leach, C.; Padmanabhan, A.; Price, C. C.; Frey, N. C.; Raizada, A.; Rajaraman, V.; Saiprasad, S. A.; Tang, X.; Vojvodic, A. MXene Materials for the Electrochemical Nitrogen Reduction—Functionalized or Not? *ACS Catal.* **2020**, *10* (1), 253–264.
- (11) Kamysbayev, V.; Filatov, A. S.; Hu, H.; Rui, X.; Lagunas, F.; Wang, D.; Klie, R. F.; Talapin, D. V. Covalent surface modifications and superconductivity of two-dimensional metal carbide MXenes. *Science* **2020**, *369* (6506), 979–983.
- (12) Jin, H.; Liu, X.; Vasileff, A.; Jiao, Y.; Zhao, Y.; Zheng, Y.; Qiao, S. Z. Single-Crystal Nitrogen-Rich Two-Dimensional  $\mathrm{Mo_5N_6}$  Nanosheets for Efficient and Stable Seawater Splitting. ACS Nano 2018, 12 (12), 12761–12769.
- (13) Ning, M. Q.; Lu, M. M.; Li, J. B.; Chen, Z.; Dou, Y. K.; Wang, C. Z.; Rehman, F.; Cao, M. S.; Jin, H. B. Two-dimensional nanosheets of MoS<sub>2</sub>: a promising material with high dielectric properties and microwave absorption performance. *Nanoscale* **2015**, *7* (38), 15734–40.

- (14) Wang, S.; Zhang, D.; Li, B.; Zhang, C.; Du, Z.; Yin, H.; Bi, X.; Yang, S. Ultrastable In-Plane 1T-2H MoS<sub>2</sub> Heterostructures for Enhanced Hydrogen Evolution Reaction. *Adv. Energy Mater.* **2018**, 8 (25), 1801345.
- (15) Liu, X.; Jiao, Y.; Zheng, Y.; Jaroniec, M.; Qiao, S. Z. Building Up a Picture of the Electrocatalytic Nitrogen Reduction Activity of Transition Metal Single-Atom Catalysts. *J. Am. Chem. Soc.* **2019**, *141* (24), 9664–9672.
- (16) Yu, H.; Yang, X.; Xiao, X.; Chen, M.; Zhang, Q.; Huang, L.; Wu, J.; Li, T.; Chen, S.; Song, L.; Gu, L.; Xia, B. Y.; Feng, G.; Li, J.; Zhou, J. Atmospheric-Pressure Synthesis of 2D Nitrogen-Rich Tungsten Nitride. *Adv. Mater.* **2018**, *30* (51), No. e1805655.
- (17) Lin, Y.; Yang, C.; Niu, Q.; Luo, S. Interfacial Charge Transfer between Silver Phosphate and  $W_2N_3$  Induced by Nitrogen Vacancies Enhances Removal of  $\beta$ -Lactam Antibiotics. *Adv. Funct. Mater.* **2022**, 32, 2108814.
- (18) Tan, S.; Tackett, B. M.; He, Q.; Lee, J. H.; Chen, J. G.; Wong, S. S. Synthesis and electrocatalytic applications of flower-like motifs and associated composites of nitrogen-enriched tungsten nitride  $(W_3N_3)$ . Nano Res. **2020**, 13 (5), 1434–1443.
- (19) Jin, H.; Li, L.; Liu, X.; Tang, C.; Xu, W.; Chen, S.; Song, L.; Zheng, Y.; Qiao, S. Z. Nitrogen Vacancies on 2D Layered  $W_2N_3$ : A Stable and Efficient Active Site for Nitrogen Reduction Reaction. *Adv. Mater.* **2019**, *31* (32), No. e1902709.
- (20) Yang, X.; Nash, J.; Anibal, J.; Dunwell, M.; Kattel, S.; Stavitski, E.; Attenkofer, K.; Chen, J. G.; Yan, Y.; Xu, B. Mechanistic Insights into Electrochemical Nitrogen Reduction Reaction on Vanadium Nitride Nanoparticles. *J. Am. Chem. Soc.* **2018**, *140* (41), 13387–13391.
- (21) Lin, J.; Wang, A.; Qiao, B.; Liu, X.; Yang, X.; Wang, X.; Liang, J.; Li, J.; Liu, J.; Zhang, T. Remarkable performance of  $Ir_1/FeO_x$  single-atom catalyst in water gas shift reaction. *J. Am. Chem. Soc.* **2013**, 135 (41), 15314–7.
- (22) Li, X.; Bi, W.; Zhang, L.; Tao, S.; Chu, W.; Zhang, Q.; Luo, Y.; Wu, C.; Xie, Y. Single-Atom Pt as Co-Catalyst for Enhanced Photocatalytic H, Evolution. *Adv. Mater.* **2016**, 28 (12), 2427–31.
- (23) Ji, S.; Chen, Y.; Fu, Q.; Chen, Y.; Dong, J.; Chen, W.; Li, Z.; Wang, Y.; Gu, L.; He, W.; Chen, C.; Peng, Q.; Huang, Y.; Duan, X.; Wang, D.; Draxl, C.; Li, Y. Confined Pyrolysis within Metal-Organic Frameworks To Form Uniform Ru<sub>3</sub> Clusters for Efficient Oxidation of Alcohols. *J. Am. Chem. Soc.* **2017**, *139* (29), 9795–9798.
- (24) Lei, Y.; Mehmood, F.; Lee, S.; Greeley, J.; Lee, B.; Seifert, S.; Winans, R. E.; Elam, J. W.; Meyer, R. J.; Redfern, P. C.; Teschner, D.; Schlogl, R.; Pellin, M. J.; Curtiss, L. A.; Vajda, S. Increased silver activity for direct propylene epoxidation via subnanometer size effects. *Science* **2010**, 328 (5975), 224–8.
- (25) Ling, C.; Ouyang, Y.; Li, Q.; Bai, X.; Mao, X.; Du, A.; Wang, J. A General Two-Step Strategy-Based High-Throughput Screening of Single Atom Catalysts for Nitrogen Fixation. *Small Methods* **2019**, 3 (9), 1800376.
- (26) Ling, C.; Niu, X.; Li, Q.; Du, A.; Wang, J. Metal-Free Single Atom Catalyst for N<sub>2</sub> Fixation Driven by Visible Light. *J. Am. Chem. Soc.* **2018**, *140* (43), 14161–14168.
- (27) He, T.; Puente Santiago, A. R.; Du, A. Atomically embedded asymmetrical dual-metal dimers on N-doped graphene for ultra-efficient nitrogen reduction reaction. *J. Catal.* **2020**, 388, 77–83.
- (28) Rodriguez, M. M.; Bill, E.; Brennessel, W. W.; Holland, P. L.  $N_2$  reduction and hydrogenation to ammonia by a molecular iron-potassium complex. *Science* **2011**, 334 (6057), 780–3.
- (29) Wang, X.; Qiu, S.; Feng, J.; Tong, Y.; Zhou, F.; Li, Q.; Song, L.; Chen, S.; Wu, K. H.; Su, P.; Ye, S.; Hou, F.; Dou, S. X.; Liu, H. K.; Lu, G. Q.; Sun, C.; Liu, J.; Liang, J. Confined Fe-Cu Clusters as Sub-Nanometer Reactors for Efficiently Regulating the Electrochemical Nitrogen Reduction Reaction. *Adv. Mater.* **2020**, 32 (40), No. e2004382.
- (30) Bai, L.; Hsu, C. S.; Alexander, D. T. L.; Chen, H. M.; Hu, X. A Cobalt-Iron Double-Atom Catalyst for the Oxygen Evolution Reaction. *J. Am. Chem. Soc.* **2019**, *141* (36), 14190–14199.

- (31) Zheng, G.; Li, L.; Tian, Z.; Zhang, X.; Chen, L. Heterogeneous single-cluster catalysts (Mn<sub>3</sub>, Fe<sub>3</sub>, Co<sub>3</sub>, and Mo<sub>3</sub>) supported on nitrogen-doped graphene for robust electrochemical nitrogen reduction. *Journal of Energy Chemistry* **2021**, *54*, 612–619.
- (32) Liu, J. C.; Ma, X. L.; Li, Y.; Wang, Y. G.; Xiao, H.; Li, J. Heterogeneous Fe<sub>3</sub> single-cluster catalyst for ammonia synthesis via an associative mechanism. *Nat. Commun.* **2018**, *9* (1), 1610.
- (33) Li, L.; Xu, L. Design of a graphene nitrene two-dimensional catalyst providing a well-defined site accommodating up to three metals, with application to  $N_2$  reduction electrocatalysis. *Chem. Commun. (Camb.)* **2020**, *56* (63), 8960–8963.
- (34) Chen, S.; Yuan, H.; Morozov, S. I.; Ge, L.; Li, L.; Xu, L.; Goddard, W. A., III. Design of a Graphene Nitrene Two-Dimensional Catalyst Heterostructure Providing a Well-Defined Site Accommodating One to Three Metals, with Application to CO<sub>2</sub> Reduction Electrocatalysis for the Two-Metal Case. *J. Phys. Chem. Lett.* **2020**, *11* (7), 2541–2549.
- (35) Diao, J.; Qiu, Y.; Liu, S.; Wang, W.; Chen, K.; Li, H.; Yuan, W.; Qu, Y.; Guo, X. Interfacial Engineering of W<sub>2</sub>N/WC Heterostructures Derived from Solid-State Synthesis: A Highly Efficient Trifunctional Electrocatalyst for ORR, OER, and HER. *Adv. Mater.* **2020**, 32 (7), No. e1905679.
- (36) Hammer, B.; Norskov, J. K. Theoretical Surface Science and Catalysis Calculations and Concepts. *Adv. Catal.* **2000**, *45*, 71–129.
- (37) Hammer, B.; Morikawa, Y.; Nørskov, J. K. CO Chemisorption at Metal Surfaces and Overlayers. *Phys. Rev. Lett.* **1996**, 76 (12), 2141–2144.
- (38) Xu, H.; Cheng, D.; Cao, D.; Zeng, X. C. A universal principle for a rational design of single-atom electrocatalysts. *Nature Catal.* **2018**, *1* (5), 339–348.
- (39) Toropov, A. A.; Toropova, A. P. QSPR Modeling of Stability of Complexes of Adenosine Phosphate Derivatives with Metals Absent from the Complexes of the Teaching Access. *Russian J. Coord. Chem.* **2001**, 27 (8), 574–578.
- (40) Calle-Vallejo, F.; Inoglu, N. G.; Su, H. Y.; Martínez, J.; Man, I. C.; Koper, M.; Kitchin, J. R.; Rossmeisl, J. Number of outer electrons as descriptor for adsorption processes on transition metals and their oxides. *Chem. Sci.* **2013**, *4* (3), 1245–1249.
- (41) Zhan, C.; Sun, W.; Xie, Y.; Jiang, D. E.; Kent, P. R. C. Computational Discovery and Design of MXenes for Energy Applications: Status, Successes, and Opportunities. *ACS Appl. Mater. Interfaces* **2019**, *11* (28), 24885–24905.
- (42) O'Connor, N. J.; Jonayat, A. S. M.; Janik, M. J.; Senftle, T. P. Interaction trends between single metal atoms and oxide supports identified with density functional theory and statistical learning. *Nature Catal.* **2018**, *1* (7), 531–539.
- (43) Fung, V.; Hu, G.; Wu, Z.; Jiang, D.-e. Descriptors for Hydrogen Evolution on Single Atom Catalysts in Nitrogen-Doped Graphene. *J. Phys. Chem. C* **2020**, *124* (36), 19571–19578.
- (44) Wang, S.; Wu, Z.; Dai, S.; Jiang, D. E. Deep Learning Accelerated Determination of Hydride Locations in Metal Nanoclusters. *Angew. Chem., Int. Ed. Engl.* **2021**, 60 (22), 12289–12292.
- (45) Wang, S.; Li, Y.; Dai, S.; Jiang, D. E. Prediction by Convolutional Neural Networks of CO<sub>2</sub> /N<sub>2</sub> Selectivity in Porous Carbons from N<sub>2</sub> Adsorption Isotherm at 77 K. Angew. Chem., Int. Ed. Engl. 2020, 59 (44), 19645–19648.
- (46) Wexler, R. B.; Martirez, J. M. P.; Rappe, A. M. Chemical Pressure-Driven Enhancement of the Hydrogen Evolving Activity of Ni<sub>2</sub>P from Nonmetal Surface Doping Interpreted via Machine Learning. *J. Am. Chem. Soc.* **2018**, *140* (13), 4678–4683.
- (47) Ge, L.; Yuan, H.; Min, Y.; Li, L.; Chen, S.; Xu, L.; Goddard, W. A., III. Predicted Optimal Bifunctional Electrocatalysts for the Hydrogen Evolution Reaction and the Oxygen Evolution Reaction Using Chalcogenide Heterostructures Based on Machine Learning Analysis of in Silico Quantum Mechanics Based High Throughput Screening. J. Phys. Chem. Lett. 2020, 11 (3), 869–876.
- (48) Ge, L.; Xu, W.; Chen, C.; Tang, C.; Xu, L.; Chen, Z. Rational Prediction of Single Metal Atom Supported on Two-Dimensional

- Metal Diborides for Electrocatalytic N<sub>2</sub> Reduction Reaction with Integrated Descriptor. *J. Phys. Chem. Lett.* **2020**, *11* (13), 5241–5247.
- (49) Min, Y.; Yuan, H.; Wang, W.; Xu, L. Design of Heterostructures of MXene/Two-Dimensional Organic Frameworks for Na-O<sub>2</sub> Batteries with a New Mechanism and a New Descriptor. *J. Phys. Chem. Lett.* **2021**, *12* (11), 2742–2748.
- (50) Yuan, H.; Min, Y.; Xu, L. Prediction of Dual-Doped Integrated CsPbBr<sub>3</sub>-CsPbCl<sub>3</sub> Perovskite Heterostructure for Practical Photocatalytic Water Splitting with a New Descriptor. *J. Phys. Chem. Lett.* **2021**, *12* (2), 822–828.
- (51) Kim, D.; Shi, J.; Liu, Y. Substantial Impact of Charge on Electrochemical Reactions of Two-Dimensional Materials. *J. Am. Chem. Soc.* **2018**, *140* (29), 9127–9131.
- (52) Zhu, X.; Zhou, X.; Jing, Y.; Li, Y. Electrochemical synthesis of urea on MBenes. *Nat. Commun.* **2021**, *12* (1), 4080.
- (53) Kresse, G.; Hafner, J. Norm-Conserving and Ultrasoft Pseudopotentials for First-Row and Transition-Elements. *J. Phys.: Condens. Matter* **1994**, *6* (40), 8245–8257.
- (54) Vanderbilt, D. Soft Self-Consistent Pseudopotentials in a Generalized Eigenvalue Formalism. *Phys. Rev. B* **1990**, *41* (11), 7892–7895.
- (55) Perdew, J. P.; Chevary, J. A.; Vosko, S. H.; Jackson, K. A.; Pederson, M. R.; Singh, D. J.; Fiolhais, C. Erratum: Atoms, molecules, solids, and surfaces: Applications of the generalized gradient approximation for exchange and correlation. *Phys. Rev. B: Condens. Matter Mater. Phys.* 1993, 48 (7), 4978.
- (56) Perdew, J. P.; Wang, Y. Accurate and simple analytic representation of the electron-gas correlation energy. *Phys. Rev. B: Condens. Matter Mater. Phys.* **1992**, *45* (23), 13244–13249.
- (57) Blochl, P. E. Projector augmented-wave method. *Phys. Rev. B: Condens. Matter Mater. Phys.* **1994**, *50* (24), 17953–17979.
- (58) Kresse, G.; Joubert, D. From ultrasoft pseudopotentials to the projector augmented-wave method. *Phys. Rev. B* **1999**, *59* (3), 1758–1775.
- (59) Grimme, S.; Antony, J.; Ehrlich, S.; Krieg, H. A consistent and accurate ab initio parametrization of density functional dispersion correction (DFT-D) for the 94 elements H-Pu. *J. Chem. Phys.* **2010**, 132 (15), 154104.
- (60) Peterson, A. A.; Abild-Pedersen, F.; Studt, F.; Rossmeisl, J.; Nørskov, J. K. How copper catalyzes the electroreduction of carbon dioxide into hydrocarbon fuels. *Energy Environ. Sci.* **2010**, 3 (9), 1311–1315.
- (61) Wang, V.; Xu, N.; Liu, J.-C.; Tang, G.; Geng, W.-T. VASPKIT: A user-friendly interface facilitating high-throughput computing and analysis using VASP code. *Comput. Phys. Commun.* **2021**, 267, 108033
- (62) Deringer, V. L.; Tchougreeff, A. L.; Dronskowski, R. Crystal orbital Hamilton population (COHP) analysis as projected from plane-wave basis sets. *J. Phys. Chem. A* **2011**, *115* (21), 5461–6.
- (63) Maintz, S.; Deringer, V. L.; Tchougreeff, A. L.; Dronskowski, R. Analytic projection from plane-wave and PAW wavefunctions and application to chemical-bonding analysis in solids. *J. Comput. Chem.* **2013**, *34* (29), 2557–67.
- (64) Maintz, S.; Deringer, V. L.; Tchougreeff, A. L.; Dronskowski, R. LOBSTER: A tool to extract chemical bonding from plane-wave based DFT. *J. Comput. Chem.* **2016**, *37* (11), 1030–5.
- (65) Nelson, R.; Ertural, C.; George, J.; Deringer, V. L.; Hautier, G.; Dronskowski, R. LOBSTER: Local orbital projections, atomic charges, and chemical-bonding analysis from projector-augmented-wave-based density-functional theory. *J. Comput. Chem.* **2020**, *41* (21), 1931–1940.
- (66) Mathew, K.; Sundararaman, R.; Letchworth-Weaver, K.; Arias, T. A.; Hennig, R. G. Implicit solvation model for density-functional study of nanocrystal surfaces and reaction pathways. *J. Chem. Phys.* **2014**, *140* (8), 9519–9825.
- (67) Sundararaman, R.; Goddard, W. A., III. The charge-asymmetric nonlocally determined local-electric (CANDLE) solvation model. *J. Chem. Phys.* **2015**, *142* (6), 064107.

(68) Sundararaman, R.; Goddard, W. A., III.; Arias, T. A. Grand canonical electronic density-functional theory: Algorithms and applications to electrochemistry. *J. Chem. Phys.* **2017**, *146* (11), 114104.

## **□** Recommended by ACS

### Ni Nanoclusters Anchored on Ni-N-C Sites for CO<sub>2</sub> Electroreduction at High Current Densities

Yanfang Song, Wei Wei, et al.

FEBRUARY 20, 2023

ACS APPLIED MATERIALS & INTERFACES

READ 🗹

### p-Block Antimony Single-Atom Catalysts for Nitric Oxide Electroreduction to Ammonia

Kai Chen, Ke Chu, et al.

FEBRUARY 03, 2023

ACS ENERGY LETTERS

READ 🗹

# Oxygen Vacancy-Reinforced Water-Assisted Proton Hopping for Enhanced Catalytic Hydrogenation

Xiaojun Zhao, You-Nian Liu, et al.

JANUARY 31, 2023

ACS CATALYSIS

READ 🗹

# Sub-nm RuO<sub>x</sub> Clusters on Pd Metallene for Synergistically Enhanced Nitrate Electroreduction to Ammonia

Xiaotian Li, Ke Chu, et al.

JANUARY 11, 2023

ACS NANO

READ **C** 

Get More Suggestions >